TU Delft

Delft University of Technology

Document Version
Final published version

Licence
Dutch Copyright Act (Article 25fa)

Citation (APA)
Foroozan, F., Ianiro, A., Discetti, S., & Baars, W. J. (2025). Resolving convective velocities of turbulent boundary layer-induced convective heat transfer fluctuations at the wall. *Physical Review Fluids*, *10*(9), 1-19. Article 094904. https://doi.org/10.1103/bs9l-bhqz

Important note
To cite this publication, please use the final published version (if applicable).
Please check the document version above.

Copyright
In case the licence states “Dutch Copyright Act (Article 25fa)”, this publication was made available Green Open Access via the TU Delft Institutional Repository pursuant to Dutch Copyright Act (Article 25fa, the Taverne amendment). This provision does not affect copyright ownership.
Unless copyright is transferred by contract or statute, it remains with the copyright holder.

Sharing and reuse
Other than for strictly personal use, it is not permitted to download, forward or distribute the text or part of it, without the consent of the author(s) and/or copyright holder(s), unless the work is under an open content license such as Creative Commons.

Takedown policy
Please contact us and provide details if you believe this document breaches copyrights.
We will remove access to the work immediately and investigate your claim.

This work is downloaded from Delft University of Technology.

Resolving convective velocities of turbulent boundary layer-induced convective heat transfer fluctuations at the wall

Firoozeh Foroozan,[1] Andrea Ianiro,[1] Stefano Discetti,[1] and Woutijn J. Baars[2,*]
[1]*Department of Aerospace Engineering, Universidad Carlos III de Madrid, 28911 Leganés, Spain*
[2]*Faculty of Aerospace Engineering, Delft University of Technology, 2629HS Delft, The Netherlands*

(Received 8 February 2025; accepted 19 August 2025; published 17 September 2025)

We demonstrate the capability to experimentally measure fluctuations of the convective heat transfer coefficient at the wall in a turbulent boundary layer. To achieve this, we measure two-dimensional fields of wall-temperature fluctuations beneath a zero-pressure-gradient turbulent boundary layer at two moderate friction Reynolds numbers ($Re_\tau \approx 990$ and $Re_\tau \approx 1800$). Spatiotemporal data of wall temperature are acquired by means of a heated-thin-foil sensor as sensing hardware and an infrared camera as a temperature detector. At the lower Re_τ condition, the fields of Nusselt number fluctuations (Nu') exhibit elongated features comprising streamwise and spanwise length scales comparable to those of near-wall streaks. At higher Re_τ, the effective width and length of the streaks of Nu fluctuations increase. These findings are based on two-point correlations as well as streamwise-spanwise energy spectra of Nu fluctuations at the wall. The convective velocities of the Nu fluctuations are also computed using the available temporal resolution. This allows for resolving the multiscale nature of convective footprints of wall-bounded turbulence: Our experimental data reflect that larger streaks in the footprint convect at velocities in the order of the free-stream velocity, whereas more energetic smaller-scale features move at velocities in the order of $10u_\tau$. Measurements of the kind presented here offer a promising method for wall-based sensing of turbulence and thus for usage as input to flow control systems.

DOI: 10.1103/bs9l-bhqz

I. INTRODUCTION

Viscous interactions between turbulence and solid boundaries directly affect mass, momentum, and energy transport. Understanding, modeling, and accurately sensing the dynamics of turbulent boundary layers (TBLs) are essential for the performance of a wide range of engineering devices. For instance, active control of TBLs requires fast, accurate, and nonintrusive sensing strategies, thus leaving the paradigm of sensing from the wall as the most appealing option [1]. Our current work focuses on the feasibility of performing time-resolved convective heat transfer measurements in a TBL flow with air as the working fluid, to infer the spatiotemporal footprint of the convecting flow. We rely on time-resolved infrared (IR) thermography, coupled with a heated-thin-foil sensor [2].

Being able to measure the footprint of wall-bounded turbulence in a nonintrusive manner is of use when implementing real-time control systems (particularly when skin-friction drag reduction is concerned, for which any form drag of sensors/actuators is detrimental for the system performance). Real-time control of off-the-wall turbulent velocity fluctuations relies on methods that estimate them using only wall data (e.g., Refs. [3–7]). Most methods require instantaneous fields of both the streamwise and spanwise components of skin friction and pressure. While those data are

*Contact author: w.j.baars@tudelft.nl

 ©2025 American Physical Society

easily accessible in numerical simulations, experimentally measuring these three quantities over a grid of points is challenging. Fortunately, recent works have suggested that only one quantity is sufficient for meaningful estimates of off-the-wall velocity fields [8,9], as was also demonstrated in experimental studies on real-time control of TBL flow [10] and on turbulence estimation from intrusive and sparse measurements [[11,12], among others].

Typically, the wall footprint of turbulence dynamics can be obtained through measurements of the unsteady wall-pressure or wall-shear stress. Low values of turbulence-induced pressure fluctuations yield a challenge for the measurement of instantaneous wall-pressure fields [13,14]. Likewise, challenges exist in the measurement of wall-shear-stress fields, e.g., with a deformable sensor, whose inertia limits the maximum measurement frequency [15]. A convective heat flux sensor offers an alternative to measuring wall-shear stress and is considered in the current work. The similarity between mean momentum and thermal energy transport in wall-bounded flows was discussed by Reynolds [16] (later reproduced in Ref. [17]). Beyond the range of validity of the Reynolds analogy for average quantities, several studies documented correlations between turbulent heat transfer fluctuations and the instantaneous state of wall-bounded turbulence [18–24]. Early experimental work with point measurements of heat transfer fluctuations reported a remarkable similarity between the conditionally sampled Reynolds heat flux and Reynolds shear stress [25]. While this similarity cannot be interpreted as evidence of causality, a quadrant analysis revealed that sweep and burst events are accompanied, with high probability, by equivalent events in the heat flux. Iritani *et al.* [26] explicitly showed that the turbulent temperature field near the wall is similar to the flow field in the near-wall region, with the aid of temperature-sensitive liquid crystals and hydrogen bubbles to visualize thermal streaks and velocity streaks, respectively. Kong *et al.* [27] confirmed this strong correlation between the existence of both thermal and velocity streaks using direct numerical simulations (DNSs) of a TBL. The spanwise spacing of the velocity and thermal streaks was estimated by means of two-point correlations and equaled 100 viscous lengths for isothermal boundary conditions. The viscous length scale, l^*, equaled ν/u_τ, with ν being the fluid kinematic viscosity and $u_\tau \equiv \sqrt{\tau_w/\rho}$ being the mean friction velocity (where τ_w is the wall-shear stress and ρ is the fluid density). Larger spacings (of approximately $150l^*$) were observed for the iso-heat-flux boundary condition, due to the breakup of equation similarity between heat and momentum. The Direct Numerical Simulations (DNS) by Abe *et al.* [28] analyzed turbulent heat transfer in channel flows at various values of the friction Reynolds number, $\mathrm{Re}_\tau \equiv u_\tau \delta/\nu$, up to a value of 640 (here δ is the boundary layer thickness). According to Abe *et al.* [28], the spanwise correlation of the wall temperature fields includes a negative peak at low Reynolds numbers, but this peak diminishes with an increase in Re_τ and is smaller than 5% at $\mathrm{Re}_\tau \approx 640$ (thus suggesting that the wall temperature field becomes more broadband). Later results by Abe *et al.* [22] confirmed this trend, providing results up to $\mathrm{Re}_\tau \approx 1020$. Abe *et al.* ascribed the lack of negative spanwise coherence in the wall-temperature field to clustering of the near-wall streaks in higher Reynolds number flows. Recent simulations were performed over an even wider range of Re_τ (reaching values of up to 5000), and for various Prandtl numbers and thermal boundary conditions [29–31]. There it was found that the intensity of thermal fluctuations increases with Re_τ.

Given the strong relation between fluctuations in wall-shear stress, τ_w (and off-the-wall turbulence quantities), and the convective heat transfer coefficient, h, it is worth exploring whether the latter could act as a surrogate for nonintrusive input data for flow estimation. Kim and Lee [24] recently utilized the strong relation between τ_w and h for predictions of turbulent heat transfer. Another utilization of the strong τ_w, h-relation was demonstrated by Miozzi *et al.* [32], who inferred the skin friction vector field around a wall-mounted cube from time-resolved temperature maps of a heated wall obtained using a functional coating of temperature-sensitive paint. Hence, the experimentally acquired convective heat transfer coefficient could be informative of the off-the-wall velocity state. For time-resolved measurements, this is also true when high-sensitivity and high-repetition-rate Infrared (IR) cameras are used. In this regard, the instantaneous heat transfer fields were measured in air by Nakamura and Yamada [33] and Raiola *et al.* [34], following the seminal work by Hetsroni and Rozenblit [18]. Synchronized measurements were also obtained with IR thermography and particle

image velocimetry (PIV) in water by Gurka *et al.* [20] and Foroozan *et al.* [35]. However, when concentrating on turbulent air flows at moderate-to-high Reynolds numbers, the higher characteristic frequencies of the turbulence, as well as the relatively small thermal conductivity of air, challenge an accurate measurement of convective heat transfer. Recent progress has been made through data analysis, such as the procedure developed by Cuéllar *et al.* [36], to ensure that the fluctuating Nusselt number Nu could be measured with an uncertainty below 10%.

The measurement of time-resolved convective heat transfer with a heated-thin-foil requires detailed measurements of wall-temperature fluctuations. As detailed in Sec. II, the wall-temperature fluctuations are the result of an energy balance over the foil, which includes, among other terms, the fluctuating heat transfer coefficient and the foil's thermal inertia. Generally speaking, a thin foil can be used for this purpose if its Fourier number (the ratio between the flow characteristic time and the timescale of heat diffusion across the foil's thickness) is much larger than one [2]. However, the amplitudes of temperature fluctuations are attenuated by the foil thermal inertia, leading to small values which are difficult to measure when high frequencies are involved. Literature studies discussed earlier are either performed at low Reynolds numbers ($\mathrm{Re}_\theta \lesssim 1000$) or in water, where the flow velocity is lower and the thermal conductivity is higher; both scenarios lead to larger temperature fluctuations for a given Reynolds number.

In the present work, we explore (1) whether it is possible to measure the fluctuating convective heat transfer coefficient in a TBL air flow with sufficient temporal resolution to resolve the temporal and spatial scales of turbulent heat transfer events and (2) how the measured spatiotemporal fields scale with Reynolds number. To achieve this, we employ high-repetition-rate IR thermography, coupled with a heated-thin-foil sensor beneath a zero-pressure-gradient (ZPG) TBL at two Reynolds numbers of $\mathrm{Re}_\tau \approx 990$ and $\mathrm{Re}_\tau \approx 1800$. Following a description of the experimental setup and the methodology in Sec. II, we discuss the spatiotemporal maps of the heat transfer coefficient in Sec. III A and statistical two-point correlations and energy spectra in Sec. III B. A frequency-wave-number spectral analysis is carried out in Sec. III C to examine the convective velocities of different streamwise scales present in the fields of Nu fluctuations.

II. EXPERIMENTAL SETUP

A. Flow setup and statistics

The experimental campaign was conducted in an open-loop wind tunnel facility within the Faculty of Aerospace Engineering at the Delft University of Technology. A short overview of the main features of the facility is provided in the foregoing. A more detailed description can be found in Refs. [10,37].

The wind tunnel has a contraction ratio of 4.7 : 1 and can attain a maximum velocity of approximately 16.5 m/s. The flow is accelerated through a contraction with an exit cross-sectional area of $0.60 \times 0.60\,\mathrm{m}^2$. A test section with a length of 3.60 m was placed downstream of the contraction exit plane. A new boundary layer developed on the bottom wall, which was suspended in the flow with the aid of a knife-edge design, forming a bleed for the inflow boundary layer. For tripping the boundary layer, P40-grit sandpaper was used on all four walls near the inlet of the test section. The ceiling of the test section was adjusted to establish a streamwise ZPG development of the TBL flow over the bottom wall.

A modular panel centered at approximately $x' = 3.00$ m ($x' = 0$ coincides with the downstream edge of the sandpaper trip) accommodated the wall-embedded heated-thin-foil sensor, as shown in Figs. 1(a) and 1(b). Experiments were performed at two distinct free-stream velocities of $U_\infty \approx 4.8$ m/s and $U_\infty \approx 9.7$ m/s and resulted in two nominal friction Reynolds numbers of $\mathrm{Re}_\tau \approx 990$ and $\mathrm{Re}_\tau \approx 1800$. These two testing conditions are further referred to as case 1 and case 2, respectively. Profiles of both the streamwise mean velocity [Fig. 2(a)] and the streamwise turbulence kinetic energy [Fig. 2(b)]—measured with hot-wire anemometry—compare well with DNS data. Most notable is the attenuation of the turbulence kinetic energy in the current data,

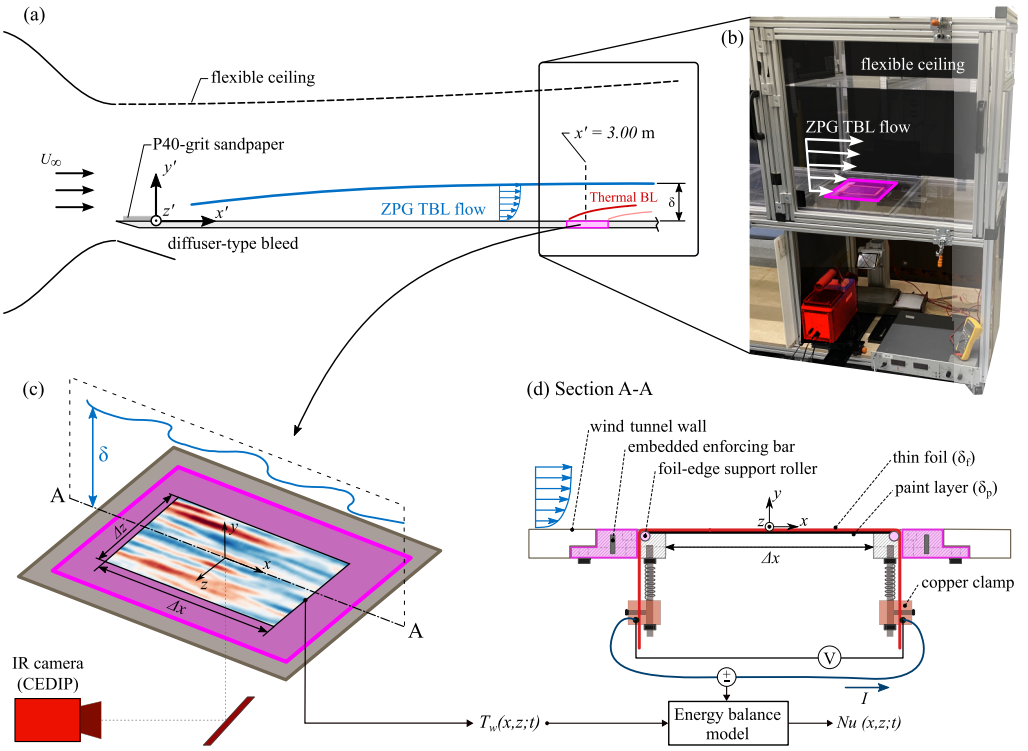

FIG. 1. (a) Schematic of the experimental setup embedded in the wind tunnel facility at the Delft University of Technology, and (b) a photograph showing the aft part of the wind tunnel facility. The setup includes an IR thermography system, imaging a heated-thin-foil sensor. (c) Schematic of the measurement area and (d) cross-sectional view of the heated-thin-foil sensor.

but this level of attenuation was ascribed to the spatial filtering by the hot-wire sensing length; see Ref. [10]. Boundary layer parameters were inferred by fitting the mean velocity profile to a composite profile with log-law constants of $\kappa = 0.384$ and $B = 4.17$ [38]. Table I reports the

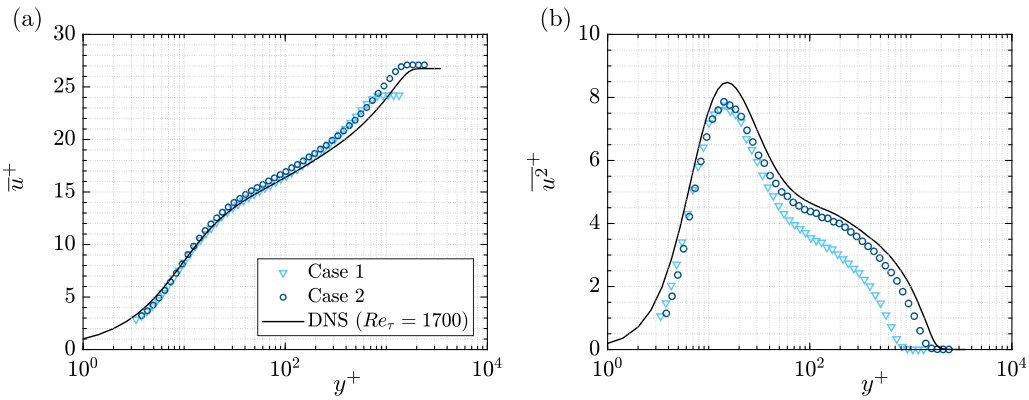

FIG. 2. Wall-normal profiles of (a) the streamwise mean velocity and (b) the streamwise turbulence kinetic energy, based on hot-wire data for cases 1 and 2 [10]. Experimental data are compared to profiles from a DNS of TBL flow [39].

TABLE I. Experimental parameters of the TBL flow at the two testing conditions and at the nominal streamwise measurement location of $x' = 3.00$ m (where the heated-thin-foil sensor was placed).

Case	U_∞ (m/s)	δ (mm)	θ (mm)	Re_θ	Re_τ	u_τ (m/s)	$l^* \equiv \nu/u_\tau$ (μm)	$t^* = \nu/u_\tau^2$ (μs)
1	4.8	72.6	6.89	2248	988	0.204	73.5	360.2
2	9.7	71.3	6.86	4572	1783	0.364	40.0	109.9

boundary layer parameters at the measurement location of $x' = 3.00$ m. Here, θ is the momentum thickness and the viscous length and timescales are denoted with symbols l^* and t^*, respectively.

B. Convective heat transfer measurement with infrared thermography

This section discusses the measurement setup and the uncertainty and limitations of the present measurement of convective heat transfer fluctuations on the wall with a flush-mounted heated-thin-foil sensor technique [40]. Schematics of the setup with this heated-thin-foil sensor are shown in Figs. 1(c) and 1(d). The setup included an IR-transparent optical path for capturing temperature fluctuations on the rear-side of the heated foil. For this, a high-sensitivity IR camera was employed (CEDIP Titanium 530L model), comprising a frame rate of up to 20 kHz. Its mercury cadmium telluride detector has a resolution of 320×256 pixels^2 and has a noise equivalent temperature difference of approximately 25 mK.

The heated-thin-foil sensor consisted of a 10-μm-thick stainless-steel foil, heated by a uniformly applied direct current across its leading and trailing edges relative to the flow. To ensure that the foil was an almost perfect emitter of radiation, the foil was coated with a thin layer of high-emissivity black paint ($\epsilon = 0.95 \pm 0.02$). The foil was classified as thermally thin based on the estimated Biot number:

$$\mathrm{Bi} = h\left(\frac{\delta_f}{k_f} + \frac{\delta_p}{k_p}\right) < 0.1, \tag{1}$$

where h is the convective heat transfer coefficient, δ_f is the thickness of the foil, k_f is the thermal conductivity of the foil, and δ_p and k_p denote the same properties but now for the black matte high-emissivity paint layer. A Biot number $\mathrm{Bi} < 0.1$ implies that the thermal resistance within the material is negligible. It can therefore be assumed that the temperature distribution across the foil's thickness was uniform. In this study, the Bi number is of the order of 10^{-4}.

Moreover, to ensure that the foil is at a uniform temperature through its thickness, also referring to the unsteady temperature variations, the Fourier number should be much larger than one, $\mathrm{Fo} \gg 1$ [2], i.e., the characteristic time of conduction through the foil should be much smaller than the characteristic time of the problem. Otherwise, the resulting temperature fluctuations might be attenuated at the higher frequencies. By taking into account both the foil and paint layers, the Fourier number can be defined as

$$\mathrm{Fo} = \frac{t_c}{\left(\frac{\delta_f}{k_f} + \frac{\delta_p}{k_p}\right)(c_f \rho_f \delta_f + c_p \rho_p \delta_p)}, \tag{2}$$

where t_c is the characteristic time of the problem which can be expressed for instance in outer units as the ratio of the boundary layer thickness and the free-stream velocity, δ/U_∞. Parameters ρ_f and ρ_p are foil and paint densities; c_f and c_p are foil and paint heat capacities, respectively. According to this modified definition, the calculated values for Fo are 6.0 and 2.9 for cases 1 and 2, respectively. This ensures that the characteristic time of conduction through the foil is smaller than the characteristic time of the problem, and thus that the temporal response is fast enough to track the typical heat transfer fluctuations in the flow. Note that the paint contribution in Eq. (2) lowers the value of the Fourier number; this suggests the need for applying (thinner) foil coatings in future works.

TABLE II. Experimental parameters related to the temporal acquisition of IR thermography images, and the spatial field-of-view captured by the images.

	Physical units			Inner units			Outer units		
Parameter		Case 1	Case 2		Case 1	Case 2		Case 1	Case 2
Acquisition rate f_s	Hz	300	500	$\frac{f_s l^*}{u_\tau}$	0.108	0.055	$\frac{f_s \delta}{U_\infty}$	4.45	3.67
Acquisition time T_s	s	60	56	$\frac{T_s u_\tau}{l^*}$	1.67×10^5	5.10×10^5	$\frac{T_s U_\infty}{\delta}$	4.04×10^3	7.62×10^3
Imaging length Δx	mm	113	113	$\frac{\Delta x}{l^*}$	1632.7	3000.0	$\frac{\Delta x}{\delta}$	1.65	1.68
Imaging width Δz	mm	66	66	$\frac{\Delta z}{l^*}$	1088.4	2000.0	$\frac{\Delta z}{\delta}$	1.10	1.12
Image resolution	px/mm	1.31	1.31	px/l^*	0.0963	0.0524	px/δ	95.106	93.403

As illustrated in the cross-sectional view of Fig. 1(d), the foil was securely stretched between a pair of copper clamps over which the voltage was applied. The clamps were fitted with compressed springs to adjust the foil tension. The heated area of the foil was calculated based on its stretched length (233 mm) between the two clamps [see the red curve in Fig. 1(d)] and its width (103 mm); this gives a heated area of $A = 2.40 \times 10^{-2}\,\mathrm{m}^2$. Note that this area is different from the measurement area, which is set by a cutout window in the sensor-support plate. This support plate was reinforced with two embedded metal bars to prevent bending due to the spring tension. To reduce contact resistance and local heating, the electrical connection between the copper and foil was achieved using 1-mm-thick indium wires placed in a triangular engraving on the surface of the copper bars. Additionally, two Teflon pipes filled with solid metal cylinders were employed as support rollers for the sensor's edges normal to the flow direction to ensure the foil remained under tension while heated [41].

A $120 \times 80\,\mathrm{mm}^2$ section was removed from the sensor-support plate to allow the acquisition of IR thermography images. This allowed the IR camera to view the foil from the non-flow-exposed side through this window cutout, while still ensuring proper support for the foil. In terms of the spatial acquisition parameters, the imaged area of the sensor was slightly smaller than the dimensions of the window cutout, comprising an imaging length and width of $\Delta x = 113\,\mathrm{mm}$ and $\Delta z = 66\,\mathrm{mm}$, respectively (the image resolution was 1.31 pixels/mm). A sample field of temperature data is sketched in Fig. 1(c), and from the cross-sectional view of Fig. 1(d) it is seen that the heated-thin-foil is larger than the measured field of view. Regarding the temporal acquisition details, the camera frame rate was set at $f_s = 300\,\mathrm{Hz}$ for case 1 (lower Re_τ) and $f_s = 500\,\mathrm{Hz}$ for case 2 (higher Re_τ). This leads to similar nondimensional acquisition frequencies when expressed in outer units ($f_s\delta/U_\infty = 4.45$ and 3.67 for cases 1 and 2, respectively, as outlined in Table II). However, since the viscous length scale is much smaller in case 2, a lower frame rate is achieved for that case when nondimensionalized in inner units ($f_s l^*/u_\tau = 0.108$ and 0.055 for cases 1 and 2, respectively). Nevertheless, as demonstrated in the results section, the acquisition frequency is deemed sufficient to capture the temporal dynamics of energetic features. Finally, data were acquired for a temporal duration of nearly 60 seconds for both cases 1 and 2, and equates to a minimum acquisition time of $T_s U_\infty/\delta \approx 4040$ boundary layer turnover times (case 1); this was checked to be sufficient for converged spectral statistics at the lowest frequencies of interest. All relevant acquisition parameters of this experiment, along with their corresponding values, are presented in Table II.

Raw measurements of temperature fluctuations require processing to yield fields of Nu fluctuations. For this, the convective heat transfer coefficient, h, of a heated foil with surface temperature T_w, surrounded by a fluid at adiabatic wall temperature T_{aw}, can be estimated through an energy balance, as given by Eq. (3). The parameters related to the heated-thin-foil sensor, along with their corresponding values and uncertainties, are presented in Table III:

$$h = \frac{\dot{q}_{\mathrm{in}} - \dot{q}_{\mathrm{cd}} - \dot{q}_{\mathrm{rd}} - B}{T_w - T_{aw}}. \tag{3}$$

TABLE III. Parameters and their values used in the energy balance model of the sensor.

Quantity	Symbol	Value	Units
Electrical current	I	14.5, 17.5 ± 0.01[a]	A
Electrical voltage	V	3.2, 3.8 ± 0.01[a]	V
Heated foil area	A	0.024 ± 2.5 × 10^{-5}	m^2
Ambient temperature	T_{amb}	24.7	°C
Thermal conductivity (foil)	k_f	16.3 ± 2	W/(m K)
Thermal conductivity (paint)	k_p	1.4 ± 0.1	W/(m K)
Thickness (foil)	δ_f	10 ± 0.1	μm
Thickness (paint)	δ_p	20 ± 0.1	μm
Heat capacity (foil)	c_f	500 ± 5	J/(kg K)
Heat capacity (paint)	c_p	5000 ± 50	J/(kg K)
Density (foil)	ρ_f	7930 ± 50	kg/m^3
Density (paint)	ρ_p	1300 ± 50	kg/m^3
Emissivity (foil)	ϵ_f	0.17 ± 0.02	
Emissivity (paint)	ϵ_p	0.95 ± 0.02	
Stefan-Boltzmann constant	σ	5.67 × 10^{-8}	$W/(m^2\ K^4)$

[a]Each of the two individual values correspond to cases 1 and 2 in the experiment.

In Eq. (3), $\dot{q}_{in}$ is the input heat flux due to Joule heating, $\dot{q}_{cd}$ is the conduction heat flux through the foil, $\dot{q}_{rd}$ is the radiation heat flux, and B is the thermal inertia term. The input heat flux, $\dot{q}_{in}$, is obtained from the Joule heating of the foil, as

$$\dot{q}_{in} = IV/A, \tag{4}$$

where I is the current applied through the foil, V is the voltage differential between the copper clamps holding the foil, and A is the surface area of the thin foil stretched between the two pairs of copper clamps. The radiation heat flux, $\dot{q}_{rd}$, is estimated using the Stefan-Boltzmann law, considering the surface emissivity ϵ of the paint layer covering the foil and assuming that the whole wind tunnel laboratory can be modeled as a blackbody at ambient temperature T_{amb}:

$$\dot{q}_{rd} = \sigma\epsilon\left(T_w^4 - T_{amb}^4\right), \tag{5}$$

where σ is the Stefan-Boltzmann constant. The lateral conduction heat flux, $\dot{q}_{cd}$, is obtained from the Laplacian of the wall temperature, multiplied by the in-plane thermal conductance:

$$\dot{q}_{cd} = -(k_f\delta_f + k_p\delta_p)\nabla^2 T_w, \tag{6}$$

where the subscripts f and p refer to foil and paint, respectively. Here, the computation of second spatial derivatives is possible thanks to the relatively high spatial resolution (1.31 pixels/mm, see Table III) of temperature measurements, although it is challenged by the measurement noise, which requires spatial filtering [34,36].

Lastly, term B in Eq. (3) represents the heat flux absorbed or released by the foil due to its heat capacity and is computed as follows:

$$B = (c_f\rho_f\delta_f + c_p\rho_p\delta_p)\left(\frac{\partial T_w}{\partial t}\right). \tag{7}$$

The temporal derivative was calculated using a central difference scheme with the frame interval as the time step. Finally, the Nusselt number was calculated from the convective heat transfer coefficient:

$$\mathrm{Nu} = \frac{h\cdot\delta}{k_a}, \tag{8}$$

with the characteristic length of the problem taken as the boundary layer thickness δ, and k_a being the thermal conductivity of air. Measurement uncertainty of Nu, estimated following the method of Moffat [42] and employing the uncertainties reported in Table III, was found to be lower than 11%.

It must be noted that fine-scale noise in the spatial-temporal distribution significantly affects the calculation of the spatial and temporal derivative terms in Eqs. (6) and (7), respectively. For instance, the accurate evaluation of the temporal derivative in Eq. (7) requires a sufficient sensor heating to obtain an acceptable signal-to-noise ratio (the ratio between temperature fluctuations and IR-camera measurement noise). However, too-large heating values may lead to a change in the local air parameters (such as density, viscosity, and Prandtl number). As such, the overheat ratio of the foil should be carefully chosen, and the interested reader is referred to Ref. [36]. Aside from the proper overheating ratio, the signal-to-noise ratio was improved by filtering the raw data with a suitable technique similar to the one applied by Cuéllar *et al.* [36]. A high-pass filter removes features with a long characteristic time of at least $250\delta/U_\infty$. This ensures that low-frequency dynamics, e.g., caused by a slow convection cell forming on the foil side that is not exposed to the flow, is removed. Additionally, following Raiola *et al.* [34], a feature-based filtering, based on proper orthogonal decomposition is employed to remove any residual measurement noise; the number of modes retained was determined using the elbow method [43]. For a detailed discussion about filtering approaches to improve the signal-to-noise ratio of temperature fluctuations, the reader is referred to Ref. [44].

A final postprocessing step was applied in relation to camera noise. Analysis of the frequency spectrum from the temporal data of the Nusselt number fluctuations revealed a consistent peak at 39 Hz ($\pm$ 2 Hz). Presumably, this peak is caused by the internal cooling system of the IR camera. This issue was previously observed on another IR camera by Meola *et al.* [45]. To eliminate this disturbance, a band-pass filter targeting the range 37 Hz to 41 Hz was applied on the time-varying, but spatially averaged temperature. This approach was performed on local patches of the image to take into account spatial non-uniformness due to the Narcissus effect [46] of the IR camera sensor.

III. RESULTS AND DISCUSSION

The results are organized into three subsections. First, samples of the instantaneous temperature and convective heat transfer maps are presented, referred to as the flow *footprint*. Second, second-order spatial statistics, comprising two-point correlations and two-dimensional (2D) energy spectra, are covered to quantify the streamwise and spanwise scales of the turbulence present within the footprint. Subsequently, a third subsection focuses on the convective velocities associated with the broadband range of scales in turbulent velocities affecting the footprint.

A. Understanding the footprint

Figure 3 reports contour plots of sample fields of the instantaneous fluctuating wall temperature, $T_w' = T_w - \overline{T_w}$, and Nusselt number $\mathrm{Nu}' = \mathrm{Nu} - \overline{\mathrm{Nu}}$. The average values, indicated with an overline, are obtained with spatial and temporal averaging of the raw temperature and Nusselt number fields, $T_w(x, z, t)$ and $\mathrm{Nu}(x, z, t)$, respectively. The origin of the x, y-coordinate system used to present the results is located at the streamwise/spanwise center of the heated-thin-foil [see the coordinate system indicated in Figs. 1(c) and 1(d)]. Axes of all subplots in Fig. 3 are expressed in inner units and comprise the same range. As such, the fixed sensor size is larger in terms of viscous units for the higher Reynolds-number data of case 2.

For the T_w' maps in Figs. 3(a) and 3(b), regions of positive temperature fluctuations generally correspond to areas of integrated reduced convective heat transfer (leading to an increase of temperature of the foil over time), while negative temperature fluctuation regions generally indicate enhanced convective heat transfer, although this correspondence is not obvious due to the unsteady term in Eq. (7), especially at high frequencies (while in slower flows this is more evident, see Ref. [35]). To quantify spatial variations in temperature, the mean and standard deviation of $T_w - T_{aw}$ were

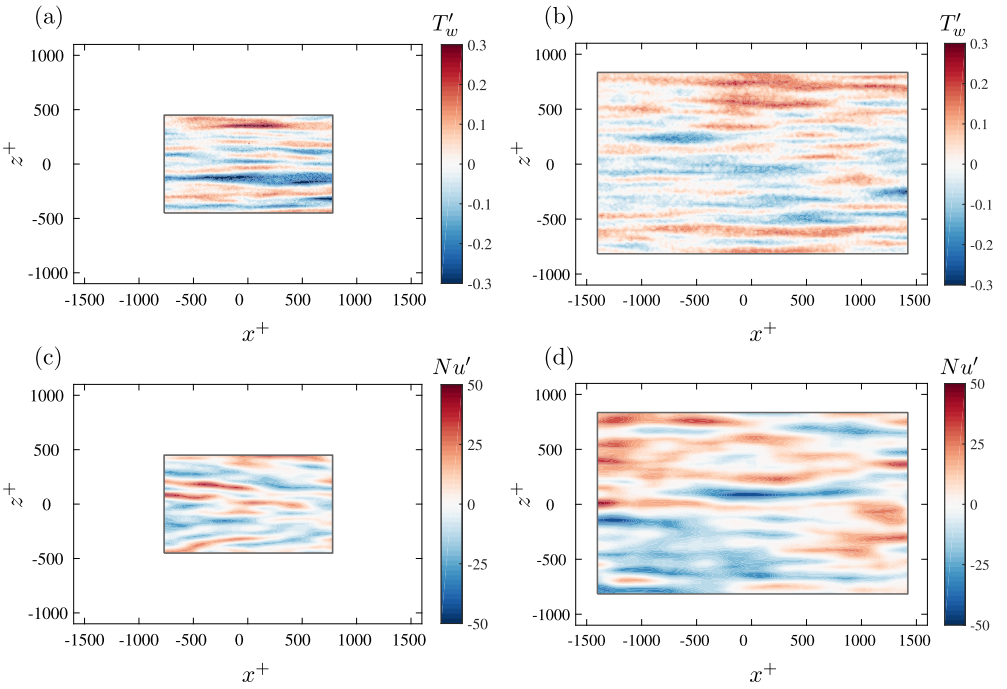

FIG. 3. (a), (b) Instantaneous maps of the wall-temperature fluctuations, T'_w, and (c), (d) of the Nusselt number fluctuations, Nu', for both case 1 (left) and case 2 (right).

calculated across the measurement area. The mean wall-temperature increase for the lower Re_τ was found to be $\overline{T_w - T_{aw}} = 55.3\,\mathrm{K}$, with a standard deviation of 0.120 K, and for the higher Re_τ was found to be $\overline{T_w - T_{aw}} = 53.8\,\mathrm{K}$, with a standard deviation of 0.091 K. While these values of heating may seem large, it should be noted that the induced buoyancy effects are negligible, since the Richardson number remains smaller than 10^{-2} (for the lower Re_τ case). The lower level of temperature fluctuations for the case at higher Re_τ, suggests a relatively minor attenuation of T'_w fluctuations due to the foil thermal inertia at higher frequencies.

The Nu' maps in Figs. 3(c) and 3(d) highlight regions of enhanced or reduced instantaneous heat transfer intensity. High values correspond to strong convective heat transfer; by assuming an analogy between Nu and the skin friction coefficient, C_f, these regions are subject to higher streamwise velocity, although synchronized velocity and heat transfer measurements are needed to verify this analogy and to quantify the (scale-dependent) phase delay between velocity fluctuations and wall heat transfer patterns.

The mean Nusselt number for the lower Re_τ case was calculated as $\overline{\mathrm{Nu}} = 68.0 \pm 5$, with a standard deviation of 16.2, and for the higher Re_τ case as $\overline{\mathrm{Nu}} = 106.5 \pm 10$, with a standard deviation of 17.0. For TBL flow, formulations found in the literature for the mean Nusselt number, $\overline{\mathrm{Nu}}$, are generally a function of the Reynolds number, based on the streamwise coordinate [47]. However, the objective of the present study is not to examine the development of the TBL flow (the streamwise extent of the measurement domain is smaller than 1.7δ) and as such easier order-of-magnitude assessments can be done by referring to correlations between $\overline{\mathrm{Nu}}$ and Re based on outer scaling. Average values of the Nusselt number are in reasonable agreement with an empirical relation from McAdams *et al.* [48]. They report a correlation for fully developed turbulent pipe flow (where the Reynolds number, Re_D, is based on the pipe diameter): $\overline{\mathrm{Nu}} = 0.023\mathrm{Re}_D^{0.8}\mathrm{Pr}^{0.4}$, of which its range of validity is $0.7 \leqslant \mathrm{Pr} \leqslant 120$ and $\mathrm{Re}_D \geqslant 10^4$. According to this correlation, the expected values for $\overline{\mathrm{Nu}}$ are 66 and 113 in cases 1 and 2, respectively. For what concerns the Nu fluctuation intensity,

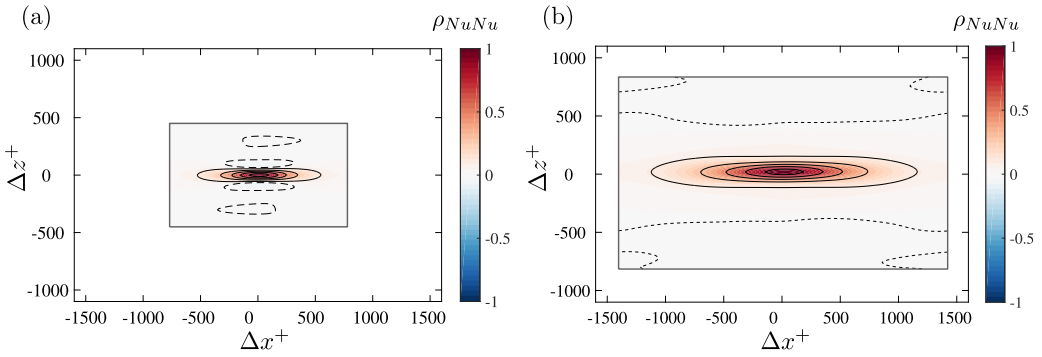

FIG. 4. Maps of the two-point correlation coefficient, ρ_{NuNu}, as defined in Eq. (9) for (a) case 1 and (b) case 2. Solid isocontours correspond to positive values of $\rho_{\mathrm{NuNu}} = 0.1 : 0.2 : 0.9$, and dashed isocontours correspond to one negative value of $\rho_{\mathrm{NuNu}} = -0.01$ (case 1) and $\rho_{\mathrm{NuNu}} = -0.0001$ (case 2).

the results by Abe *et al.* [22]—who report wall-temperature fluctuations—suggest that they should increase proportionally to the average Nusselt number. The only small increase in the standard deviation of Nu (17.0 in case 2 versus 16.2 in case 1) suggests an attenuation of high-frequency features due to the lower Fourier number of the sensor [Eq. (2)] in the higher-Re_τ case (further addressed in Sec, III B).

When inspecting the pattern of temperature fluctuations, elongated streaks are seen and this reflects the well-known occurrence of streaks populating the near-wall region of TBL flow. In the Nu' contour maps, streaks exhibit a spanwise spacing of approximately $150l^*$ and $300l^*$ at the lower- and higher-Reynolds numbers, respectively. Our present visualization of streaky patterns in the wall fields enriches a long-standing trend in the literature on near-wall flow visualization of elongated streaks [49–52]. The streaks demonstrate a wide range of lengths, some are found to exceed $1000l^*$ at both Reynolds numbers. The spanwise spacing, larger than the classical $\mathcal{O}(100l^*)$ of velocity streaks is in agreement with the finding by Kong *et al.* [27] for iso-heat-flux boundary conditions and with those of Abe *et al.* [22,28], claiming a larger streak width for a higher Reynolds number.

B. Time-averaged spatial statistics of the footprint

To statistically quantify the spatial patterns in the Nu' fields of Fig. 3, second-order statistics are considered in terms of two-point correlations and two-dimensional energy spectra. Two-point correlations are considered following the normalized correlation coefficient, defined as

$$\rho_{\mathrm{NuNu}}(\Delta x, \Delta z) = \frac{\langle \mathrm{Nu}'(x, z, t)\mathrm{Nu}'(x + \Delta x, z + \Delta z, t)\rangle_t}{\overline{\mathrm{Nu}'^2}}, \tag{9}$$

where $\langle \dots \rangle_t$ indicates ensemble averaging in time and the denominator is the variance evaluated based on the entire dataset (i.e., computed in space and time).

Both two-point correlation maps in Fig. 4 show a streamwise-elongated arrangement, surrounded by shallow negative peaks, and agree with the literature, e.g., Refs. [22,28,53]. The elongated correlation region shown for the lower Re_τ, becomes longer and thicker for the higher Re_τ; in this case, the negative values for the correlation map within the observed region become smaller, confirming the trend expected by Abe *et al.* [28] for increasing Re_τ.

2D energy spectra are computed to assess the distributions of spatial scales. Here, the spectrum is taken according to

$$\phi_{\mathrm{NuNu}}(\lambda_x, \lambda_z) = \langle \widetilde{\mathrm{Nu}}(\lambda_x, \lambda_z; t)\rangle_t, \tag{10}$$

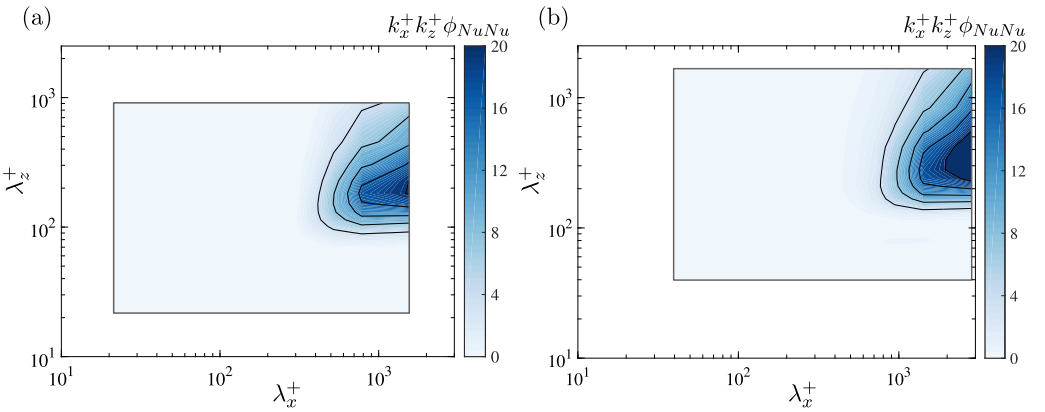

FIG. 5. Premultiplied two-dimensional energy spectra of Nusselt number fluctuations, $k_x^+k_z^+\phi_{\mathrm{NuNu}}$ for (a) case 1 and (b) case 2. Solid isocontours correspond to levels of $k_x^+k_z^+\phi_{\mathrm{NuNu}} = 4 : 4 : 20$.

with the tilde indicating the two-dimensional Fourier transform in both spatial directions, e.g., $\widetilde{\mathrm{Nu}}(\lambda_x, \lambda_z; t) = \mathcal{F}[Nu(x, z, t)]$. Two-dimensional spectra are shown in Fig. 5 for both cases 1 and 2. As before, both subplots comprise axes scaled with inner units, spanning a similar range, and thus the data cover different regions due to the fixed physical sensor size and resolution of the IR camera. At the lower Re_τ, most energy in the 2D spectrum resides at a spanwise wavelength of approximately $\lambda_z^+ = 150$. This result is in agreement with literature studies for iso-heat-flux boundary conditions [27]. Such a wavelength is larger than the typical $100l^*$ width of near-wall streaks and is similar to the wavelengths observed for the temperature fluctuations further from the wall in thermal boundary layers with isothermal boundary conditions. For instance, when qualitatively comparing the current results to the available literature (albeit differences in flow parameters), the spatial spectra of temperature fluctuations are similar to those reported by Balasubramanian *et al.* [54] for $\mathrm{Pr} = 1$, a wall-normal distance of $y^+ = 30$, and a lower Reynolds number. Nevertheless, this qualitative comparison implies that the measured Nu fields are the footprint of several hierarchies of coherent flow features, spanning different sizes and wall-normal extents. Corroborating this argument, for the higher Re_τ, the dominant spanwise wavelength is roughly $\lambda_z^+ = 300$ to 350. This increase of the spanwise wavelength with increasing Reynolds number is consistent with the results reported by Li *et al.* [53].

When focusing on the energy distribution of case 1, as a function of the streamwise wavelength, the dominant region of energy resides at wavelengths larger than approximately $\lambda_x^+ = 1500$ (larger than the streamwise length of the sensor). At the higher Re_τ, the dominant wavelength shifts to even higher wavelengths ($\lambda_x^+ \gtrsim 3000$). At the same time, the level of energy grows. This shift and growth in energy is expected for the larger scale separation and increased heat transfer intensity at higher Reynolds numbers.

It is important to note that the spatial resolution of the IR camera and the dimensions of the sensors used can impose certain limitations on the ability to effectively capture and analyze both very small and very large scales. Overall, the results presented in the foregoing demonstrate the ability of the nonintrusive heated-thin-foil sensor to capture the (mean) convective heat-transfer coefficient in a TBL air flow as well as the spatial structure of streamwise-elongated streaks in the footprint of the TBL flow. When an inner-normalization is used, this structure is *not* invariant with Re_τ. This is due to a combination of an attenuation of the smaller-scale fluctuations in velocity and wall-shear stress in the higher Re_τ scenario (case 2, comprising less sensor resolution in viscous units). In addition, for the higher Re_τ, the large-scale velocity fluctuations in the TBL flow are more energetic and consequently have a greater energy content in the measured footprint.

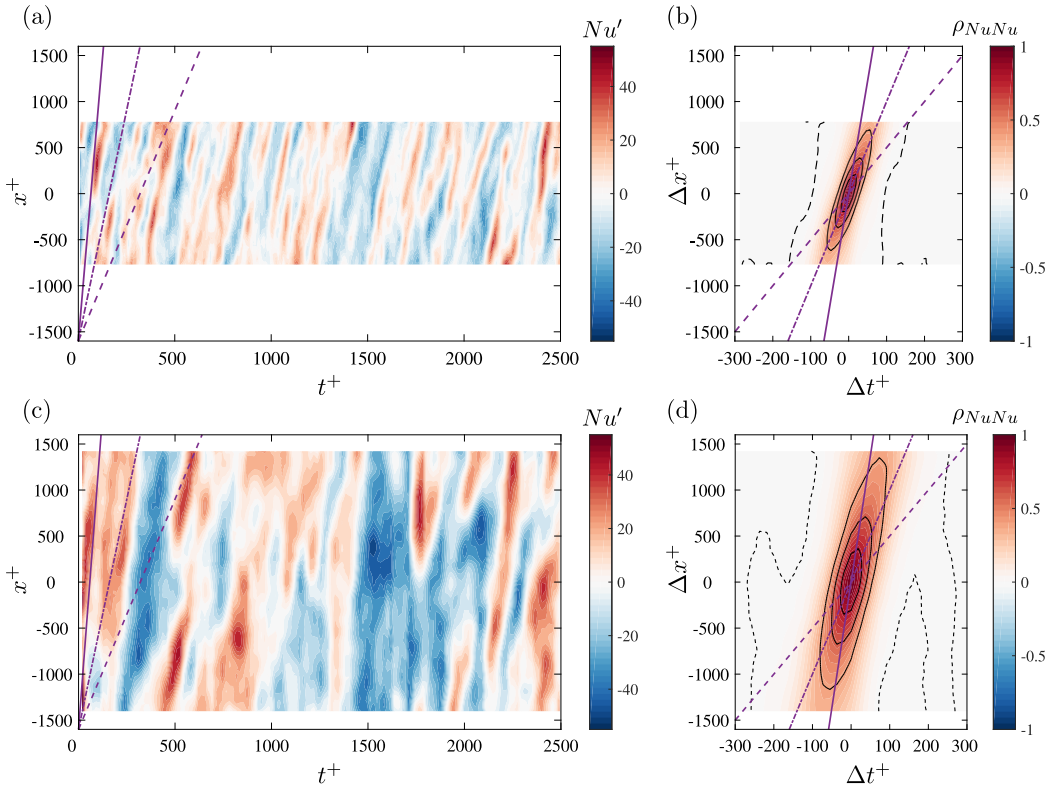

FIG. 6. (a), (c) Space-time contour maps of Nu fluctuations at the midspan of the sensor ($z = 0$) and (b), (d) maps of the two-point correlation coefficient, ρ_{NuNu} for both case 1 (top row) and case 2 (bottom row). Within the two-point correlation maps, solid isocontours correspond to positive values of $\rho_{\mathrm{NuNu}} = 0.4 : 0.2 : 0.8$, and dashed isocontours correspond to one negative value of $\rho_{\mathrm{NuNu}} = -0.01$. In all subplots, trend lines are included to indicate constant convective velocities of $U_c = 5u_\tau$ (- - -), $U_c = 10u_\tau$ (— —), and $U_c = U_\infty$ (——).

C. Inferring the convective velocity of the footprint

The temporal evolution of the spatial footprint can be assessed to study how the flow-induced pattern of the footprint convects downstream. A raw visualization of the convective pattern is shown in Fig. 6, in which the space-time maps of Nu′ are shown over a short time interval (fixed range in terms of t^+) for both case 1 [Fig. 6(a)] and case 2 [Fig. 6(c)]. These space-time contours are shown for the midspan of the Nu′ field, so for $\mathrm{Nu}'(x^+, z = 0, t^+)$. Persistent streaky structures are observed over the domain and their slopes depict the convective velocities of the wall-footprint.

Several methods to determine the convective velocity, U_c, of turbulent structures have been applied in the literature, e.g., Refs. [28,55–58]. Using space-time separations, the convective velocity of coherent structures can be estimated by identifying their convective length and time, after which the convective velocity is simply taken as $U_c = \Delta x/\Delta t$. This approach assumes that turbulent eddies are convected downstream without significant deformation over short time (or length) scales. The applicability of this method relying on Taylor's hypothesis has been extensively reviewed in the literature [59,60].

The space-time correlations can be generated from the spatiotemporal data to obtain preliminary estimates of U_c values. Space-time correlations are generated following Eq. (9), but with a temporal offset instead of a spatial (spanwise) one, to yield $\rho_{\mathrm{NuNu}}(\Delta x, \Delta t)$. Results are shown in Figs. 6(b) and 6(d), corresponding to cases 1 and 2, respectively. The inclined isocontours of the two-point

correlation maps reveal that the convective velocities vary for different turbulent length scales; the convective velocity is thus scale dependent (broadband). Even though all scale-dependent information is masked due to various scales contributing to the correlation for a certain offset (Δx and Δt), the two-point correlation maps still exhibit the general trend of the dispersive convective pattern. That is, the elongated contours in the streamwise direction suggest that large-scale turbulent structures maintain coherence over extended distances. In Figs. 6(b) and 6(d), three trend lines are shown for different convective velocities (listed in the caption). Isocontours of relatively high values (e.g., $\rho_{\mathrm{NuNu}} = 0.8$) are largely influenced by the presence of small turbulent scales. These isocontours possess space-time slopes that are relatively close to the trend line of $5u_\tau$ (the isocontours have a slope of roughly $7u_\tau$ to $8u_\tau$), as the small scales are convected at speeds close to the local mean velocity near the wall. In contrast, isocontours of relatively low values (e.g., $\rho_{\mathrm{NuNu}} = 0.4$) adhere to higher convective velocities in excess of $10u_\tau$. A similar result was presented by Abe *et al.* [22] for $\mathrm{Re}_\tau = 1020$, where DNSs of turbulent heat transfer was carried out in a channel flow. The dispersive trends align with previous findings such as with those by del Álamo and Jiménez [61], who reported similar scale-dependent velocities in DNSs of TBL flow. They suggested that, while the convective velocity of the small scales is similar to the mean velocity above $y^+ \approx 10$ to 15, the convective velocity of the large scales is closer to the free-stream velocity even in the near-wall region. Similar conclusions regarding the dispersive convective velocities of turbulent scales have been well-established with identical approaches applied to hot-wire data of turbulent flow, e.g., Refs. [55,62,63].

Literature has shown that the convective velocity is strongly scale dependent [64], especially for scales that are most energetic in the near-wall region. It is possible to retain scale information by considering the space-time correlation in the frequency-wave-number domain. For this, we employ the frequency-wave-number spectrum, taken from the data at one specific z_i location as

$$\phi_{\mathrm{NuNu}}(f, \lambda_x) = \langle \widetilde{\mathrm{Nu}}(\lambda_x, z_i; t) \rangle_z, \tag{11}$$

with the tilde here indicating the two-dimensional Fourier transform along the dimensions of space (in x) and time, e.g., $\widetilde{\mathrm{Nu}}(f, \lambda_x) = \mathcal{F}[\mathrm{Nu}(x, z_i, t)]$. Ensemble averaging is performed in time and also by considering all z_i locations. Frequency-wave-number spectra are presented in pre-multiplied form in Figs. 7(b) and 7(e). Here, straight trend lines are representative of various convective velocities, since $U_c = \frac{2\pi f}{k_x}$ with f being the temporal frequency and k_x being the spatial wave number in x.

Trends that are revealed in Figs. 7(b) and 7(e) extend the preliminary observations based on Figs. 6(b) and 6(d): spatiotemporal features in the Nu' maps that are most energetic convect at velocities in the order of $10u_\tau$. However, the total resolved energy of Nu' is distributed in a broadband manner in the frequency-wave-number space and thus indicates a dispersive field. In particular, the fluctuations in Nu' that are more elongated in x (residing at small wave numbers, k_x) comprise a wide spread of convection velocities. Their spread ranges from values below $5u_\tau$ up to almost the free-stream velocity, U_∞. Smaller spatial scales (say in the order of $k_x\delta = 10$) do not convect at speeds faster than $10u_\tau$, as the energy vanishes on the right-hand-side of the $U_c = 10u_\tau$ trend line [in both Figs. 7(b) and 7(e)]. On the other hand, larger spatial scales convect faster; the energy of streamwise-elongated fluctuations being convected at larger velocities is larger at higher Re_τ. These results of the frequency-wave-number spectra allow us to claim that the features observed in the Nu' maps measured at the wall are the footprint of velocity scales populating a large wall-normal range of the boundary layer. Those who extend further from the wall are more elongated in x and convect at larger velocities. Because of the outer-scale normalization used, the results are relatively indifferent at the large-scale/low-frequency side of the spectra.

According to Wills [55] the frequency-wave-number (f, k_x) spectrum can be used to obtain another measure of convective velocity that is a function of the wave number. Figure 8 follows this analysis by presenting the probability density function (PDF) of f, k_x-spectra for bands of

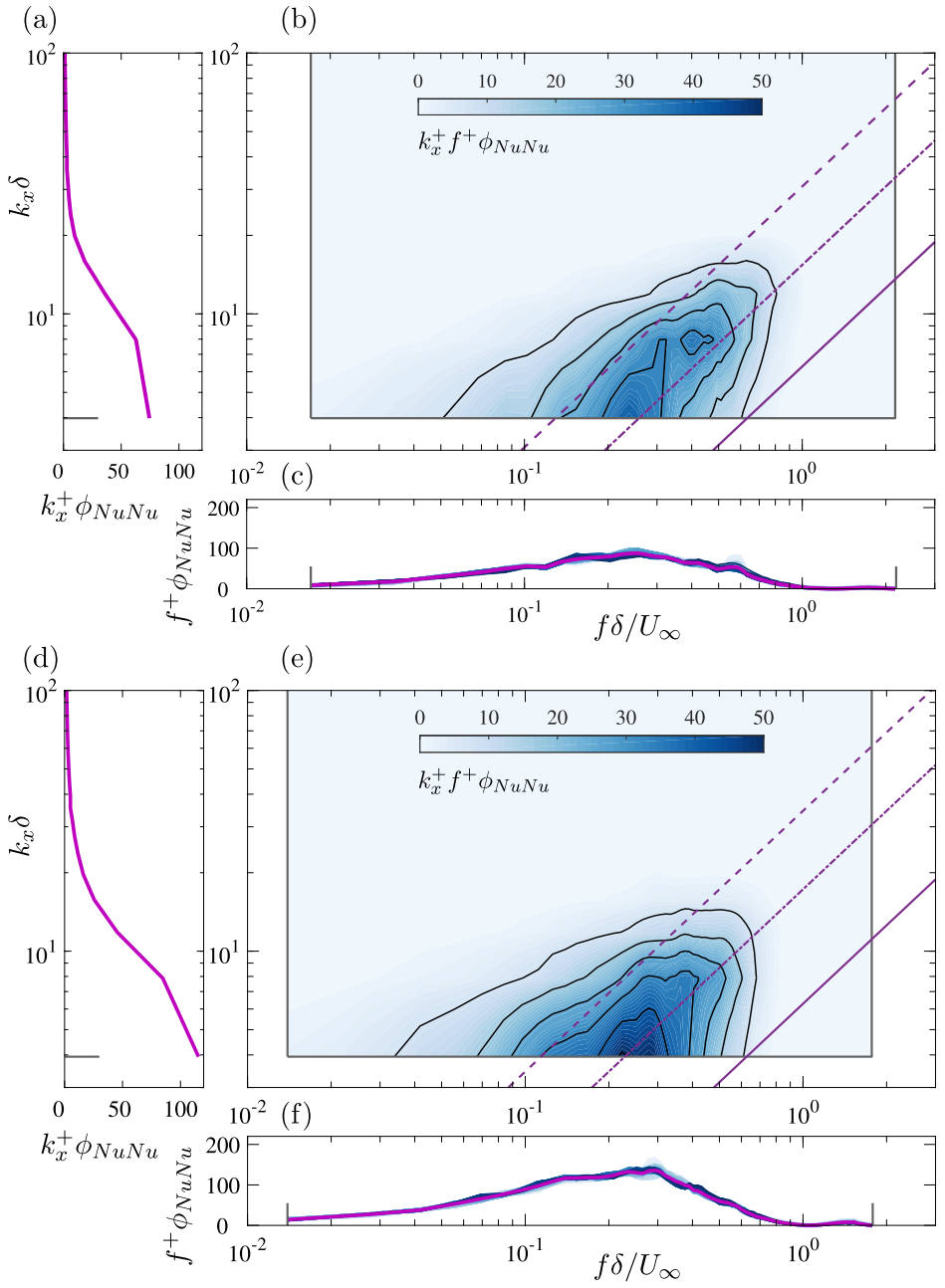

FIG. 7. Premultiplied frequency-wave-number spectra, $k_x^+ f^+ \phi_{\mathrm{NuNu}}$, for (b) case 1 and (e) case 2. Trend lines are included to indicate constant convective velocities of $U_c = 5u_\tau$ (- - -), $U_c = 10u_\tau$ (— · —), and $U_c = U_\infty$ (——). Premultiplied one-dimensional energy spectra are also included: (a), (d) wave-number spectra, and (c), (f) frequency-spectra obtained by integrating out one direction of the frequency-wave-number spectra. Note that the frequency spectra in (c), (f) include spectra of each x location, with the bundle of blue lines as well as their average (purple line).

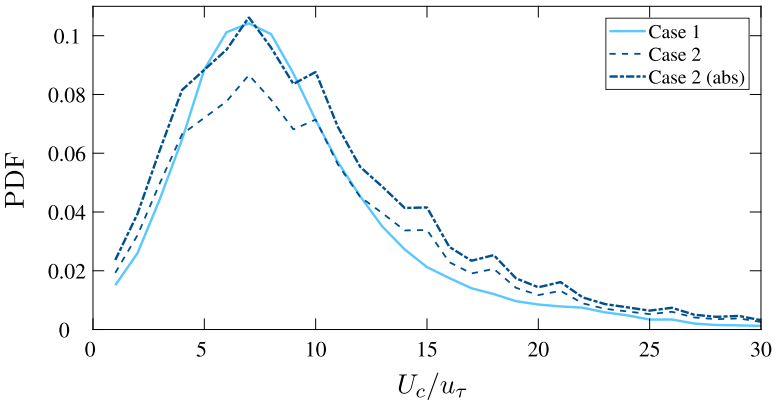

FIG. 8. Probability density functions of the frequency-wave-number spectra in bands of $U_c/u_\tau \pm 1$. The curve labeled case 2 (abs) follows Eq. (12) but with the summation in the denominator of Eq. (12) taken from case 1, so the distributions can be compared in absolute terms.

convective velocity, in terms of U_c/u_τ, with a width of $w = 1$. The PDF function is calculated as

$$\mathrm{PDF}(U_c/u_\tau) = \frac{\sum_{k_x/f=m-w/2}^{m+w/2} \phi_{\mathrm{NuNu}}(k_x, f)}{\sum \phi_{\mathrm{NuNu}}(k_x, f)} \cdot w. \tag{12}$$

Through this approach, the contribution to the total energy content from scales moving at certain convective velocities can be examined. From Fig. 8, we can infer that the bulk of the energy moves at convective velocities centered around $7u_\tau$. And so, most of the turbulent activity contributing to the observed heat transfer at the wall originates from turbulent velocity fluctuations convecting within this velocity range. From the velocity profiles in Fig. 2, we can hypothesize that such fluctuations of velocity are predominantly located below $y^+ = 50$. These findings are consistent with the interpretation that the dominant energy in the wall-normal direction originates from the near-wall region, where smaller turbulent velocity scales contribute significantly to the convective heat transfer. When inspecting the Reynolds number trend, comparing the PDFs of cases 1 and 2 can be done by considering the absolute energy growth. For this, the curve case 2 (abs) is constructed by using the energy of case 1 for the normalization in Eq. (12). This ensures that the comparison includes the growth in absolute energy of Nusselt number fluctuations, Nu' (this energy growth was evident from Figs. 5 and 7). Seemingly, at the higher Reynolds number, the amount of energy in Nu' convecting at larger velocities is greater, confirming the earlier observations based on Figs. 6(b), 6(d), 7(b), and 7(e).

IV. CONCLUSIONS

This study demonstrates the potential of a nonintrusive sensing technique for characterizing the TBL footprint through the analysis of wall-temperature fluctuations. Using a high-repetition-rate IR thermography system, combined with a heated-thin-foil sensor embedded within the wall, we successfully captured the spatiotemporal dynamics of convective heat transfer beneath a zero-pressure-gradient TBL flow at two Reynolds numbers of $\mathrm{Re}_\tau \approx 990$ and $\mathrm{Re}_\tau \approx 1800$.

Our current results reveal that the Nusselt number fluctuations, Nu', are representative of the footprint that one expects from the pattern of velocity fluctuations in the near-wall region of a TBL. It is, however, important to note that the study was not designed to inspect the one-to-one correspondence between Nu' patterns and turbulent flow features. At both Reynolds numbers, streamwise-elongated streaks were observed with dominant spanwise wavelengths of approximately 150 viscous length scales (at $\mathrm{Re}_\tau \approx 990$) and 300 viscous length scales (at $\mathrm{Re}_\tau \approx 1800$). These

streaks represent not only near-wall structures populating the near-wall region, but also the footprint of larger, wall-attached features, confirming the increasing role of large-scale turbulence with higher Reynolds numbers.

A two-dimensional spectral analysis of the Nu′ fields identified distinct turbulent scales. The streamwise length of the heated-thin-foil sensor sets an upper bound to the maximum streamwise length captured by the measurement, which equals approximately 1600 and 3000 viscous length scales for the low and high Re_τ cases, respectively. In both cases, the spectral analysis suggests that the dominant streamwise wavelengths are larger than the heated-thin foil sensor. While the spatial resolution of the sensor system is adequate to resolve the most dominant spanwise wavelength of the streaky patterns (given the agreement with the literature), the present limitation of the streamwise extent of the sensor prevents us from resolving the most energetic (large) streamwise wavelengths in Nu′ fields. In addition, the small-scale features remain attenuated due to the sensor's temporal response.

Convective velocity estimation further elucidated the convective nature of the spatiotemporal wall footprint. Large-scale structures were found to convect at speeds close to the free-stream velocity (U_∞), while smaller-scale features exhibited lower velocities, consistent with the local mean flow velocity. Specifically, at $\mathrm{Re}_\tau \approx 1800$, the convective velocity of large structures was approximately $0.8U_\infty$, while smaller structures exhibited velocities ranging from $0.4U_\infty$ to $0.6U_\infty$.

Although the current resolution adequately captures the dominant turbulent features present in the flow, there remains a significant opportunity for enhancement, especially considering the attenuation of high-frequency, fine-scale turbulence. Future work should focus on improving sensor resolution to capture finer-scale turbulence. Addressing these challenges could further enhance the utility of nonintrusive sensing for turbulence analysis and real-time control. Furthermore, the availability of synchronized flow field measurements within the boundary layer, e.g., with Particle Image Velocimetry (PIV) or hot-wire/cold-wire measurements, would be instrumental for (1) inferring correlations between instantaneous velocity fluctuations in the TBL flow and the Nu′ fields, and (2) training flow-state estimators so the heated-thin-foil sensor can be applied for predictive purposes.

In conclusion, this study demonstrates the effectiveness of nonintrusive sensing techniques in capturing the complex dynamics of boundary layer turbulence and heat transfer. The findings offer valuable insights into the spatial and temporal scales of turbulent structures, their convective velocities, and their impact on convective heat transfer. These findings are paving the way to targeted flow control strategies, as they prove we can identify flow scales from the footprint of the convective heat transfer.

ACKNOWLEDGMENTS

This activity was supported by the project ARTURO, funded by the Spanish State Research Agency, Ref. No. PID2019-109717RB-I00/AEI/10.13039/501100011033, and by the project EXCALIBUR (Grant No PID2022-138314NB-I00), funded by MCIU/AEI/10.13039/501100011033 and by ERDF: A way of making Europe. F.F. was partially supported by the UC3M mobility program. We thank R. Castellanos for assisting with the design of the heated-thin-foil sensor. We also express gratitude to the technicians of the Flow Physics & Technology laboratory within the Faculty of Aerospace Engineering at the Delft University of Technology for assistance in setting up the experiments. Finally, we acknowledge G. Dacome and F. Schrijer for contributing to the characterization of the TBL flow and to the acquisition setup of the IR camera, respectively.

DATA AVAILABILITY

The data that support the findings of this article are openly available [65].

[1] L. N. Cattafesta and M. Sheplak, Actuators for active flow control, Annu. Rev. Fluid Mech. **43**, 247 (2011).
[2] T. Astarita and G. M. Carlomagno, *Infrared Thermography for Thermo-Fluid-Dynamics* (Springer Science & Business Media, Heidelberg, Germany, 2012).
[3] A. Güemes, S. Discetti, and A. Ianiro, Sensing the turbulent large-scale motions with their wall signature, Phys. Fluids **31**, 125112 (2019).
[4] M. P. Encinar and J. Jiménez, Logarithmic-layer turbulence: A view from the wall, Phys. Rev. Fluids **4**, 114603 (2019).
[5] A. Güemes, S. Discetti, A. Ianiro, B. Sirmacek, H. Azizpour, and R. Vinuesa, From coarse wall measurements to turbulent velocity fields through deep learning, Phys. Fluids **33**, 075121 (2021).
[6] L. Guastoni, A. Güemes, A. Ianiro, S. Discetti, P. Schlatter, H. Azizpour, and R. Vinuesa, Convolutional-network models to predict wall-bounded turbulence from wall quantities, J. Fluid Mech. **928**, A27 (2021).
[7] A. Cuéllar, A. Güemes, A. Ianiro, Ó. Flores, R. Vinuesa, and S. Discetti, Three-dimensional generative adversarial networks for turbulent flow estimation from wall measurements, J. Fluid Mech. **991**, A1 (2024).
[8] A. Cuéllar, A. Ianiro, and S. Discetti, Some effects of limited wall-sensor availability on flow estimation with 3D-GANs, Theor. Comput. Fluid Dyn. **38**, 729 (2024).
[9] L. Guastoni, A. G. Balasubramanian, F. Foroozan, A. Güemes, A. Ianiro, S. Discetti, P. Schlatter, H. Azizpour, and R. Vinuesa, Fully convolutional networks for velocity-field predictions based on the wall heat flux in turbulent boundary layers, Theor. Comput. Fluid Dyn. **39**, 13 (2025).
[10] G. Dacome, R. Mörsch, M. Kotsonis, and W. J. Baars, Opposition flow control for reducing skin-friction drag of a turbulent boundary layer, Phys. Rev. Fluids **9**, 064602 (2024).
[11] F. Kerhervé, S. Roux, and R. Mathis, Combining time-resolved multi-point and spatially-resolved measurements for the recovering of very-large-scale motions in high Reynolds number turbulent boundary layer, Exp. Therm Fluid Sci. **82**, 102 (2017).
[12] S. Discetti, G. Bellani, R. Örlü, J. Serpieri, C. Sanmiguel Vila, M. Raiola, X. Zheng, L. Mascotelli, A. Talamelli, and A. Ianiro, Characterization of very-large-scale motions in high-Re pipe flows, Exp. Therm Fluid Sci. **104**, 1 (2019).
[13] M. Pastuhoff, D. Yorita, K. Asai, and P. H. Alfredsson, Enhancing the signal-to-noise ratio of pressure sensitive paint data by singular value decomposition, Meas. Sci. Technol. **24**, 075301 (2013).
[14] F. Gu, S. Discetti, Y. Liu, Z. Cao, and D. Peng, Denoising image-based experimental data without clean targets based on deep autoencoders, Exp. Therm Fluid Sci. **156**, 111195 (2024).
[15] O. Amili and J. Soria, A film-based wall shear stress sensor for wall-bounded turbulent flows, Exp. Fluids **51**, 137 (2011).
[16] O. Reynolds, On the extent and action of the heating surface of steam boilers, Proc. Manchester Literacy Philos. Soc. **14**, 7 (1874).
[17] O. Reynolds, On the extent and action of the heating surface of steam boilers, Int. J. Heat Mass Transf. **3**, 163 (1961).
[18] G. Hetsroni and R. Rozenblit, Heat transfer to a liquid—solid mixture in a flume, Int. J. Multiphase Flow **20**, 671 (1994).
[19] E. R. Meinders, K. Hanjalic, and R. J. Martinuzzi, Experimental study of the local convection heat transfer from a wall-mounted cube in turbulent channel flow, J. Heat Transf. **121**, 564 (1999).
[20] R. Gurka, A. Liberzon, and G. Hetsroni, Detecting coherent patterns in a flume by using PIV and IR imaging techniques, Exp. Fluids **37**, 230 (2004).
[21] R. A. Antonia, L. V. Krishnamoorthy, and L. Fulachier, Correlation between the longitudinal velocity fluctuation and temperature fluctuation in the near-wall region of a turbulent boundary layer, Int. J. Heat Mass Transf. **31**, 723 (1988).
[22] H. Abe, H. Kawamura, and Y. Matsuo, Surface heat-flux fluctuations in a turbulent channel flow up to $\mathrm{Re}_\tau = 1020$ with $\mathrm{Pr} = 0.025$ and 0.71, Int. J. Heat Fluid Flow **25**, 404 (2004).
[23] H. Abe and R. A. Antonia, Near-wall similarity between velocity and scalar fluctuations in a turbulent channel flow, Phys. Fluids **21**, 025109 (2009).

[24] J. Kim and C. Lee, Prediction of turbulent heat transfer using convolutional neural networks, J. Fluid Mech. **882**, A18 (2020).
[25] A. Perry and P. Hoffmann, An experimental study of turbulent convective heat transfer from a flat plate, J. Fluid Mech. **77**, 355 (1976).
[26] Y. Iritani, N. Kasagi, and M. Hirata, Heat transfer mechanism and associated turbulence structure in the near-wall region of a turbulent boundary layer, in *Turbulent Shear Flows 4,* edited by L. J. S. Bradbury, F. Durst, B. E. Launder, F. W. Schmidt, and J. H. Whitelaw (Springer, Berlin, 1985), pp. 223–234.
[27] H. Kong, H. Choi, and J. S. Lee, Direct numerical simulation of turbulent thermal boundary layers, Phys. Fluids **12**, 2555 (2000).
[28] H. Abe, H. Kawamura, and Y. Matsuo, Direct numerical simulation of a fully developed turbulent channel flow with respect to the Reynolds number dependence, J. Fluids Eng. **123**, 382 (2001).
[29] S. Pirozzoli, M. Bernardini, and P. Orlandi, Passive scalars in turbulent channel flow at high Reynolds number, J. Fluid Mech. **788**, 614 (2016).
[30] F. Alcántara-Ávila and S. Hoyas, Direct numerical simulation of thermal channel flow for medium–high Prandtl numbers up to $\mathrm{Re}_\tau = 2000$, Int. J. Heat Mass Transf. **176**, 121412 (2021).
[31] F. Alcántara-Ávila, S. Hoyas, and M. J. Pérez-Quiles, Direct numerical simulation of thermal channel flow for $\mathrm{Re}_\tau = 5000$ and $\mathrm{Pr} = 0.71$, J. Fluid Mech. **916**, A29 (2021).
[32] M. Miozzi, A. Schröder, D. Schanz, C. E. Willert, C. Klein, and J. Lemarechal, Skin-friction from temperature and velocity data around a wall-mounted cube, Exp. Fluids **65**, 156 (2024).
[33] H. Nakamura and S. Yamada, Quantitative evaluation of spatio-temporal heat transfer to a turbulent air flow using a heated thin-foil, Int. J. Heat Mass Transf. **64**, 892 (2013).
[34] M. Raiola, C. S. Greco, M. Contino, S. Discetti, and A. Ianiro, Towards enabling time-resolved measurements of turbulent convective heat transfer maps with IR thermography and a heated thin foil, Int. J. Heat Mass Transf. **108**, 199 (2017).
[35] F. Foroozan, A. Güemes, M. Raiola, R. Castellanos, S. Discetti, and A. Ianiro, Synchronized measurement of instantaneous convective heat flux and velocity fields in wall-bounded flows, Meas. Sci. Technol. **34**, 125301 (2023).
[36] A. Cuéllar, E. Amico, J. Serpieri, G. Cafiero, W. J. Baars, S. Discetti, and A. Ianiro, Measuring time-resolved heat transfer fluctuations on a heated-thin foil in a turbulent channel airflow, Meas. Sci. Technol. **36**, 045303 (2025).
[37] W. J. Baars, G. Dacome, and M. Lee, Reynolds-number scaling of wall-pressure–velocity correlations in wall-bounded turbulence, J. Fluid Mech. **981**, A15 (2024).
[38] K. A. Chauhan, P. A. Monkewitz, and H. M. Nagib, Criteria for assessing experiments in zero pressure gradient boundary layers, Fluid Dyn. Res. **41**, 021404 (2009).
[39] J. A. Sillero, J. Jiménez, and R. D. Moser, Two-point statistics for turbulent boundary layers and channels at Reynolds numbers up to $\delta^+ \approx 2000$, Phys. Fluids **26**, 105109 (2014).
[40] H. Nakamura, Frequency response and spatial resolution of a thin foil for heat transfer measurements using infrared thermography, Int. J. Heat Mass Transf. **52**, 5040 (2009).
[41] R. Castellanos, A. Ianiro, and S. Discetti, Genetically-inspired convective heat transfer enhancement in a turbulent boundary layer, Appl. Therm. Eng. **230**, 120621 (2023).
[42] R. J. Moffat, Describing the uncertainties in experimental results, Exp. Therm Fluid Sci. **1**, 3 (1988).
[43] R. B. Cattell, The scree test for the number of factors, Multiv. Behav. Res. **1**, 245 (1966).
[44] I. Robledo, J. Alfaro, C. Sanmiguel Vila, and R. Castellanos, Unsteady convective heat transfer of an impinging sweeping jet: A discussion on the effect of spatiotemporal filtering, Exp. Therm Fluid Sci. **169**, 111526 (2025).
[45] C. Meola, S. Boccardi, and G. M. Carlomagno, Measurements of very small temperature variations with LWIR QWIP infrared camera, Infrared Phys. Techn. **72**, 195 (2015).
[46] J. W. Howard and I. R. Abel, Narcissus: reflections on retroreflections in thermal imaging systems, Appl. Opt. **21**, 3393 (1982).
[47] J. H. Lienhard, Heat transfer in flat-plate boundary layers: A correlation for laminar, transitional, and turbulent flow, J. Heat Transfer. **142**, 061805 (2020).

[48] W. H. McAdams, T. K. Sherwood, and R. L. Turner, Heat transmission from condensing steam to water in surface condensers and feedwater heaters, J. Fluids Eng. **48**, 1233 (1926).
[49] S. J. Kline, W. C. Reynolds, F. A. Schraub, and P. W. Runstadler, The structure of turbulent boundary layers, J. Fluid Mech. **30**, 741 (1967).
[50] C. R. Smith and S. P. Metzler, The characteristics of low-speed streaks in the near-wall region of a turbulent boundary layer, J. Fluid Mech. **129**, 27 (1983).
[51] J. C. Klewicki, M. M. Metzger, E. Kelner, and E. M. Thurlow, Viscous sublayer flow visualizations at $\mathbf{R}_\theta \approx 1\,500\,000$, Phys. Fluids **7**, 857 (1995).
[52] A. J. Smits, B. J. McKeon, and I. Marusic, High-Reynolds number wall turbulence, Annu. Rev. Fluid Mech. **43**, 353 (2011).
[53] Q. Li, P. Schlatter, L. Brandt, and D. S. Henningson, DNS of a spatially developing turbulent boundary layer with passive scalar transport, Int. J. Heat Fluid Flow **30**, 916 (2009).
[54] A. G. Balasubramanian, L. Guastoni, P. Schlatter, and R. Vinuesa, Direct numerical simulation of a zero-pressure-gradient turbulent boundary layer with passive scalars up to Prandtl number $\mathrm{Pr} = 6$, J. Fluid Mech. **974**, A49 (2023).
[55] J. A. B. Wills, On convection velocities in turbulent shear flows, J. Fluid Mech. **20**, 417 (1964).
[56] H. Choi and P. Moin, On the space-time characteristics of wall-pressure fluctuations, Phys. Fluids A: Fluid **2**, 1450 (1990).
[57] J. Kim and F. Hussain, Propagation velocity of perturbations in turbulent channel flow, Phys. Fluids A: Fluid **5**, 695 (1993).
[58] S. Jeon, H. Choi, J. Y. Yoo, and P. Moin, Space-time characteristics of the wall shear-stress fluctuations in a low-Reynolds-number channel flow, Phys. Fluids **11**, 3084 (1999).
[59] J. Del Álamo and J. Jiménez, Estimation of turbulent convection velocities and corrections to Taylor's approximation, J. Fluid Mech. **640**, 5 (2009).
[60] P. Moin, Revisiting Taylor's hypothesis, J. Fluid Mech. **640**, 1 (2009).
[61] J. del Álamo and J. Jiménez, Scaling of the energy spectra of turbulent channels, J. Fluid Mech. **500**, 135 (2004).
[62] V. W. Goldschmidt, M. F. Young, and E. S. Ott, Turbulent convective velocities (broadband and wavenumber dependent) in a plane jet, J. Fluid Mech. **105**, 327 (1981).
[63] P. Krogstad, J. H. Kaspersen, and S. Rimestad, Convection velocities in a turbulent boundary layer, Phys. Fluids **10**, 949 (1998).
[64] C. Liu and D. F. Gayme, An input-output based analysis of convective velocity in turbulent channels, J. Fluid Mech. **888**, A32 (2020).
[65] F. Foroozan, A. Ianiro, S. Discetti, and W. J. Baars, Data underlying the publication: Resolving convective velocities of turbulent boundary layer-induced convective heat transfer fluctuations at the wall (2025), https://doi.org/10.4121/dff20e81-709f-4ed4-8853-4280ef29d066.v1.